Hindawi Publishing Corporation
Mathematical Problems in Engineering
Volume 2013, Article ID 784239, 11 pages
http://dx.doi.org/10.1155/2013/784239

Research Article

Hysteresis Phenomenon in the Galloping of the D-Shape Iced Conductor

Bin Liu, KuanJun Zhu, XinMin Li, and XuePing Zhan

China Electric Power Research Institute, Beijing 100192, China

Correspondence should be addressed to Bin Liu; liubinliubin@yeah.net

Received 5 June 2013; Revised 16 October 2013; Accepted 19 October 2013

Academic Editor: Stefano Lenci

It is well known that there is a hysteresis phenomenon in the amplitude variation in the iced conductor galloping with the wind velocity, which will have more obvious disadvantages to the overhead transmission lines. But hysteresis characteristics in the conductor galloping have not received much attention. In this paper, a continuum model of the conductor galloping with D-shape ice is derived by using Hamilton principle, where the initial deformation, the geometric nonlinearity caused by the large deformation, and the aerodynamic nonlinearity are considered. The aerodynamic forces are described by using the quasi steady hypothesis, where the aerodynamic coefficients are expanded by the polynomial curves with a third order and a ninth order, respectively. The hysteresis phenomenon is analyzed by using the approximate solutions of the Galerkin discretized equation derived from the continuum model by means of the harmonic balance method. The influence of the different factors, dynamic angle of attack, span length, initial tension, and conductor mass, is obtained in different galloping instability intervals. And two important aspects about the point of the hysteresis phenomenon onset and the size of the hysteresis region over the wind velocities are analyzed under different conditions.

1. Introduction

It is well known that iced conductor galloping is a typical low-frequency self-excited vibration phenomenon [1]. Conductor galloping represents a classical motion instability mechanism in the steady flow over a noncircular cross-section caused by ice accretion on the conductor. This conductor motion is characterized by large amplitude (possibly > 10) and low frequency (approximately 0.1–3 Hz) [2]. Although conductor galloping trace has usually an elliptical orbit on field observations, the predominant motion in galloping is vertical. Galloping can cause various kinds of structural and electrical damages in overhead lines, which can have devastating economic and social consequences [3, 4].

Conductor galloping has been studied extensively over a half century since Den Hartog [5] firstly established the vertical galloping mechanism using the quasi steady hypothesis to describe the linearized aerodynamic forces based on a simple single degree-of-freedom (DOF) model. Whereafter Nigol and Buchan [6, 7] proposed a torsional galloping mechanism based on a two-DOFs model coupled with vertical and torsional oscillations. And Yu et al. [8, 9] obtained a torsional feedback mechanism using a three-DOFs model coupled with vertical, horizontal, and torsional oscillations. And later, with the development of linear and nonlinear motion instability theories, galloping phenomenon has been studied widely by using nonlinear vibration methods [10–14].

At present, the Den Hartog theory and the torsional theory are still the two important and dominant mechanisms to explain the phenomenon of conductor galloping. The torsional theory shows that the torsional motion has a considerable effect on the instability and that its coupling with the vertical motion is responsible for most cases of the conductor galloping phenomenon [15], which is the main difference with the Den Hartog theory. So it can be excited based on Den Hartog mechanism when the torsional motion does not occur in the process of conductor galloping. And if the torsional motion is observed, the conductor galloping may be initiated by torsional theory. Especially for the bundled conductor, vertical-torsional coupling is usually the most significant to lead to galloping because of the close proximity of the natural frequencies between vertical and torsional motion. This has been verified experimentally by a number of investigators [16]. In this study, only the vertical vibration

is considered in order to discuss the hysteresis phenomenon more conveniently for the more complex nonlinear dynamic problem after the conductor galloping has appeared. And the initial conditions of conductor galloping are obtained by Den Hartog mechanism.

There are numerous examples of fundamental solutions to the conductor galloping problem as a nonlinear motion instability process [10–14]. The main objectives are usually the prediction of the stability of such aeroelastic systems at a range of flow conditions, the amplitudes, and frequencies of the Limit Cycle Oscillation (LCO) that may be encountered. And most of the efforts in galloping vibration researches have been focused on blunt bodies with regular square [17], rectangular [18, 19], or triangular cross-sections [20, 21]. But the iced-coated conductor on the transmission lines may have asymmetric complicated shapes that can usually be simplified as D-shape, U-shape, or other complex shapes, in which D-shape iced conductor is well known to induce high galloping amplitudes [4, 22].

In fact, it may still present more complex nonlinear dynamic characteristics such as bifurcation, hysteresis, and chaos, after the conductor galloping phenomenon starts off, which is significant equally to understand the galloping mechanisms [13, 17, 23–27]. Qin et al. [14] analyzed the bifurcation phenomenon for D-shape iced conductor galloping with a two-DOFs model by singularity theory. And they concluded that hysteresis phenomenon is probably obtained after LCO appeared based on appropriate parameters. Luo et al. [17] studied the square cylinder galloping phenomenon with different Reynolds number. And the results showed that the existence of intermittent shear layer reattachment leads to the existence of a hysteresis region. Barrero-Gil et al. [27] revealed the existing link between the hysteresis phenomenon and the number of inflection points at the aerodynamic force coefficient curve by means of the method of Krylov-Bogoliubov. And the bluff body was modeled by a linear oscillator of one DOF. Alonso et al. [28] demonstrated that hysteresis takes place at the angles of attack where there are inflection points in the lift coefficient curve based on the isosceles triangular cross-section bodies.

The hysteresis effect is observed in some field observations after the onset of conductor galloping. In a specific range of wind velocity, the galloping amplitude and mode present severe variation. For instance, the galloping amplitude that suddenly increases a few times will cause more serious impact to the transmission lines. It is apparent that the hysteresis phenomenon presented in the galloping response will be a more severe disadvantage to the overhead transmission lines than the only LCO onset. So understanding of the hysteresis phenomenon in the conductor galloping is important and meaningful not only in theory, but also in the development of the antigalloping methods for the transmission lines. Although many researchers have been focused on these galloping features, the hysteresis phenomenon in the conductor galloping has not been given enough attention to date. In this paper, in order to analyze the hysteresis phenomenon in conductor galloping, a continuum model that describes approximately the conductor galloping phenomenon is constructed by using Hamilton principle and considering the initial location and the geometric nonlinearity caused by the large deformation and the aerodynamic nonlinearity caused by the flow. The aerodynamic forces of D-shape iced conductor are described by using the quasi-steady hypothesis. And as a contrast, the aerodynamic coefficients are expanded by the polynomial curves with a third order and a ninth order, respectively. The hysteresis phenomenon is analyzed by using the approximate solution by means of the harmonic balance method. Then the influence of the different factors, dynamic angle of attack, span length, initial tension, and conductor mass, is proposed in different galloping instability intervals. And two important aspects about the point of the hysteresis phenomenon onset and the size of the hysteresis region over the wind velocities are analyzed under different conditions.

2. Construction of the Model

2.1. Continuum Model. The schematic diagram of the transmission line under initial tension T_0 is shown in Figure 1(a). The initial configuration $y_0(x)$ can be expressed simply using parabolic shape function as

$$y_0(x) = -\frac{4bx(l-x)}{l^2}, \tag{1}$$

where b is the sag at the lowest point of the line and l is the span length. The line is modeled as a flexible centerline with rigid cross-sections shown in Figure 1(c) which is orthogonal to the axis. This configuration is planar that belongs to the vertical plane (x- y). And α is the modification of the angle of attack introduced by the vertical velocity $\dot{y}$.

The displacement of an arbitrary line element dx is described schematically in Figure 1(b). PP_1 is the initial position with the line vector $d\vec{r}_0$ and $P'P_1'$ is the movement position with the changed vector $d\vec{r}$ taken from the line at the time Δt. And suppose that the displacements of the start and the end in x and y directions are $u(x,t)$, $v(x,t)$, and $u+u_x dx$, $v+v_x dx$, respectively. Using arc length formula and neglecting the higher-order terms of the axial deformation, the expression of the line element strain, ε_s, can be derived as

$$\varepsilon_s = u_x + \frac{dy_0}{dx}v_x + \frac{1}{2}v_x^2, \tag{2}$$

where the right subscript "x" indicates differentiation with respect to coordinate x.

Then the equations of the line motion are obtained by employing Hamilton principle [29], for example,

$$\int_{t_1}^{t_2} (\delta T - \delta V + \delta W)\, dt = 0, \tag{3}$$

where δ is the first-order variational operator, T and V are the total kinetic and strain energies, respectively, and W is

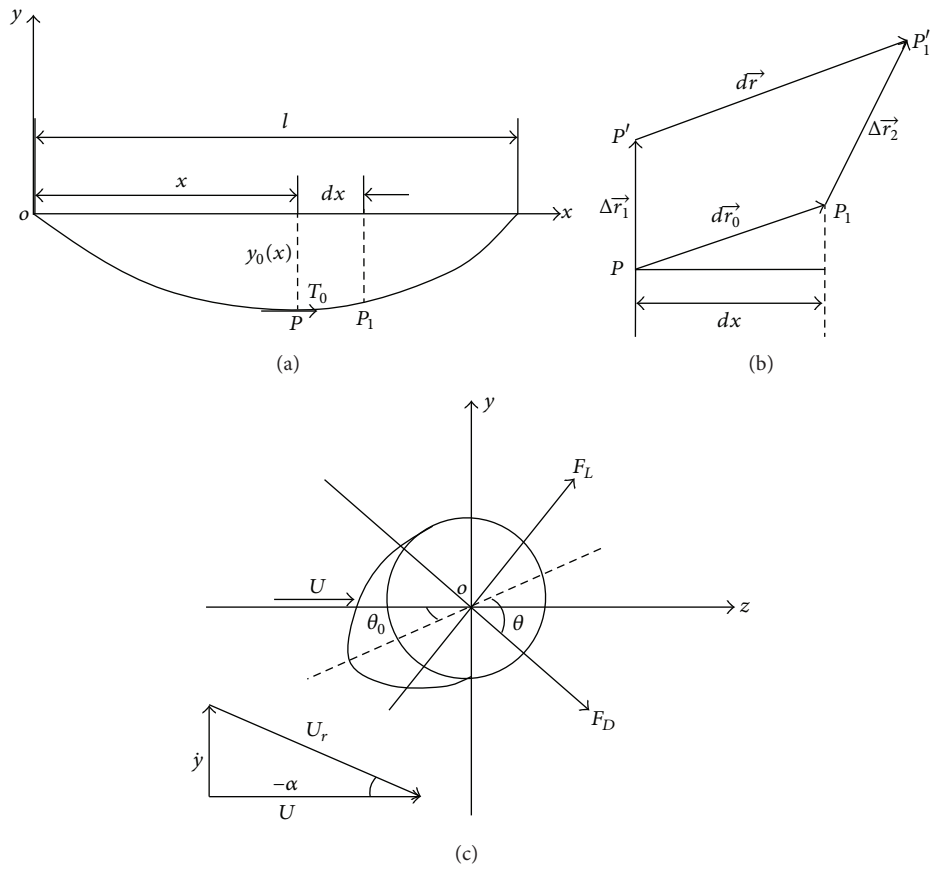

Figure 1: Model of the transmission line.

the work done by the nonconservative forces. And the T, V, and W are given by

$$V = \int_0^l \left(T_0\varepsilon_s + \frac{1}{2}EA\varepsilon_s^2\right)dx,$$
$$T = \frac{1}{2}\int_0^l m\left(\dot{u}^2 + \dot{v}^2\right)dx,$$
$$W = \int_0^l \left(F_y v - c_0\dot{v}v\right)dx, \tag{4}$$

where m is the mass per unit length, E is the elastic modulus, A is the cross-section area, F_y is the external load done by the aerodynamic force, c_0 is the damping coefficient, and a dot superscript indicates differentiation with respect to time t.

Substituting (2.1), (2), and (1) into (3) and omitting axial inertial force, the line motion equation can be obtained [14, 30] as

$$m\ddot{v} - T_0 v'' - \frac{EA}{l}\left(\frac{-8b}{l^2} + v_{xx}\right) \times \int_0^l \left(\frac{4bl - 8bx}{l^2}v_x + \frac{1}{2}v_x^2\right)dx + c_{01}\dot{v} - F_y = 0. \tag{5}$$

From (5), it is evident that the line galloping equation introduces the initial stress, the geometric nonlinearity caused by the large deformation, and the aerodynamic nonlinearity caused by the flow. So it is difficult to solve the continuum model directly.

2.2. Aerodynamic Force Model. Figure 1(c) shows a typical shape of a typical ice accretion on the conductor surface, which is observed frequently in the case of freezing rain. In Figure 1(c), F_D and F_L are the aerodynamic lift and drag due to wind actions. These forces depend on the dimensionless drag coefficient C_D and lift coefficient C_L, respectively, and have the expressions:

$$F_D = \frac{1}{2}\rho U^2 D C_D, \qquad F_L = \frac{1}{2}\rho U^2 D C_L, \tag{6}$$

where ρ is the density of the flow, U is the absolute wind velocity perpendicular to the conductor axis in the horizontal direction, and D is the reference length of the iced cross-section that is usually substituted by the conductor diameter. Then from Figure 1(c), considering the angle of attack as a relatively small amount, the aerodynamic force in y direction can be calculated as

$$F_y = F_L\cos(-\alpha) - F_D\sin(-\alpha) \approx F_L - F_D\frac{\dot{v}}{U}. \tag{7}$$

The wind forces acting on the iced conductor can be measured in wind tunnels on stationary models by resorting

to the quasi-steady theory. This theory assumes that the aerodynamic forces acting on the iced conductor at any instant in motion are identical to that on the stationary conductor under the same flow condition. And the use of the quasi-steady theory is justified because the frequencies of conductor galloping are much lower than the vortex shedding frequencies.

So the curves of the aerodynamic coefficients are obtained by the wind tunnel tests based on the stationary iced conductors at different angles of incidences. In order to establish the aerodynamic model conveniently, the polynomial curve is applied to fit onto the force coefficients versus the angle of attack by using the experimental data. Then drag coefficient C_D and lift coefficient C_L can be expressed as

$$C_L = \sum_{i=0}^{k} c_{1i}\theta^i, \qquad C_D = \sum_{i=0}^{k} c_{2i}\theta^i, \tag{8}$$

where c_{1i} and c_{2i} are the fitting coefficients of the lift and drag coefficient curves, respectively, and k is the order of the polynomial. From Figure 1(c), θ is the dynamic angle of attack based on the quasi-steady theory, which is relative to the initial static offset angle θ_0 of the iced conductor (initial ice position on the conductor) and the instantaneous angle of α, and it can be expressed as

$$\theta = \theta_0 - (-\alpha) = \theta_0 - \operatorname{arctg}\frac{\dot{v}}{U} \approx \theta_0 - \frac{\dot{v}}{U}. \tag{9}$$

In the major applications of the existing literatures, the third-order polynomial fitting formula is most widely used. But Parkinson et al. [23, 24] studied to fit by the different order polynomials. And they found that the seventh-order polynomial has superiority over the fifth order, because the former can capture the inflection point of the aerodynamic coefficient curve which is probably the pivotal factor to excite hysteresis phenomenon. The work of Ng et al. [25] has already demonstrated that a seventh-order polynomial curve used in the quasi-steady theory was sufficient in revealing the square-cylinder galloping characteristics including the hysteresis phenomenon.

In this study, assume that the eccentric ice distributed along the line is uniform and neglect the aerodynamic couples. And the third-order and the ninth-order polynomials are all selected to fit on the aerodynamic coefficient curves of D-shape eccentric iced conductor. Then the contrast by using different-order polynomials can be obtained.

Substituting (6)–(9) into (5), the motion equation can be transformed:

$$\begin{aligned} &m\ddot{v} - T_0 v_{xx} - \frac{EA}{l}\left(\frac{-8b}{l^2} + v_{xx}\right) \\ &\quad\times \int_0^l \left(\frac{4bl - 8bx}{l^2} v_x + \frac{1}{2} v_x^2\right) dx + c_{01}\dot{v} \\ &\quad - \frac{1}{2}\rho U^2 D\left[\sum_{i=0}^{k} c_{1i}\theta^k - \sum_{i=0}^{k} c_{2i}\theta^k\left(\frac{\dot{v}}{U}\right)\right] = 0. \end{aligned} \tag{10}$$

Neglecting the terms higher than third order, (10) is expanded into

$$\begin{aligned} &m\ddot{v} - T_0 v_{xx} - \frac{EA}{l}\left(\frac{-8b}{l^2} + v_{xx}\right) \\ &\quad\times \int_0^l \left(\frac{4bl - 8bx}{l^2} v_x + \frac{1}{2} v_x^2\right) dx \\ &\quad + c_1\dot{v} + d_1\dot{v}^2 + d_2\dot{v}^3 = 0. \end{aligned} \tag{11}$$

When $k = 3$, there are

$$\begin{aligned} c_1 &= c_{01} + \frac{1}{2}\rho UD\left[c_{11} + c_{20} + (2c_{12} + c_{21})\alpha_0 \right. \\ &\qquad \left. + (3c_{13} + c_{22})\alpha_0^2 + c_{23}\alpha_0^3\right], \\ d_1 &= \frac{1}{2}\rho D\left[-c_{21} - c_{12} - (3c_{13} + 2c_{22})\alpha_0 \right. \\ &\qquad \left. -3c_{23}\alpha_0^2\right], \\ d_2 &= \frac{1}{2U}\rho D\left(c_{13} + c_{22} + 3c_{23}\alpha_0\right). \end{aligned} \tag{12}$$

When $k = 9$, there are

$$\begin{aligned} c_1 &= c_{01} + \frac{1}{2}\rho UD \\ &\quad\times \left[c_{11} + c_{20} + (2c_{12} + c_{21})\alpha_0 + (3c_{13} + c_{22})\alpha_0^2 \right. \\ &\qquad + (4c_{14} + c_{23})\alpha_0^3 + (5c_{15} + c_{24})\alpha_0^4 \\ &\qquad + (6c_{16} + c_{25})\alpha_0^5 + (7c_{17} + c_{26})\alpha_0^6 \\ &\qquad \left. + (8c_{18} + c_{27})\alpha_0^7 + (9c_{19} + c_{28})\alpha_0^8 + c_{29}\alpha_0^9\right], \\ d_1 &= \frac{1}{2}\rho D \\ &\quad\times \left[-c_{12} - c_{21} - (3c_{13} + 2c_{22})\alpha_0 - (6c_{14} + 3c_{23})\alpha_0^2 \right. \\ &\qquad - (10c_{15} + 4c_{24})\alpha_0^3 - (15c_{16} + 5c_{25})\alpha_0^4 \\ &\qquad - (21c_{17} + 6c_{26})\alpha_0^5 - (28c_{18} + 7c_{27})\alpha_0^6 \\ &\qquad \left. - (36c_{19} + 8c_{28})\alpha_0^7 - 9c_{29}\alpha_0^8\right], \\ d_2 &= \frac{1}{2U}\rho D \\ &\quad\times \left[c_{13} + c_{22} + (4c_{14} + 3c_{23})\alpha_0 + (10c_{15} + 6c_{24})\alpha_0^2 \right. \\ &\qquad + (20c_{16} + 10c_{25})\alpha_0^3 + (35c_{17} + 15c_{26})\alpha_0^4 \\ &\qquad + (56c_{18} + 21c_{27})\alpha_0^5 + (84c_{19} + 28c_{28})\alpha_0^6 \\ &\qquad \left. + 36c_{29}\alpha_0^7\right]. \end{aligned} \tag{13}$$

2.3. Discrete Model. Due to solving (11), it will be approximated by using the Galerkin procedure and expanding

the displacement field in a series of suitable functions. So according to the Galerkin method, the displacement $v(x,t)$ can be expressed with the expansion:

$$v(x,t) = \sum_{i=1}^{n} q_i(t)\,\phi_i(x), \tag{14}$$

where $q_i(t)$ is the generalized amplitude time law, $\phi_i(x)$ is a set of shape functions that satisfy the geometric boundary conditions ($\phi_i(0) = \phi_j(l) = 0$), and n is the number of shape functions.

In the displacement expansion, the use of the eigenfunctions is often the best choice in the aspects of convergence and accuracy [12, 31, 32]. But in order to concentrate the study of the hysteresis phenomenon of the vertical conductor galloping, a simplified Galerkin procedure is presented by using a sine series of the antisymmetric in-plane modes as assumed shape functions [33]; that is, $\phi_i(x) = \sin(2i\pi x/l)$.

And for the sake of decreasing the number of motion equations and achieving an analytical expression to discuss the nonlinear behavior of the hysteresis phenomenon, the first-order discretization is selected. Then the discretized equation from (11) can be derived as

$$\ddot{q}_1 + Kq_1 + C\dot{q}_1 + N_1 q_1^2 + N_2 q_1^3 + N_3 \dot{q}_1^2 + N_4 \dot{q}_1^3 = 0, \tag{15}$$

where

$$K = \frac{T_0\pi^2}{l^2 m} + \frac{512b^2EA}{\pi^2 l^4 m},$$
$$C = \frac{c_1}{m}, \qquad N_1 = \frac{24b\pi EA}{l^4 m}, \qquad N_2 = \frac{\pi^4 EA}{4l^4 m}, \tag{16}$$
$$N_3 = \frac{8d_1}{3\pi m}, \qquad N_4 = \frac{3d_2}{4m}.$$

From (15), both quadratic and cubic nonlinearities appear in the displacement and velocity terms.

3. Analytical Solution of the Galloping Equation

In the work of Vio et al. [13], six common methods were compared with each other to predict bifurcation and LCO amplitudes of the transverse galloping for a square section beam. They found that two methods, higher-order harmonic balance and numerical continuation, can fully and accurately characterize the problem. So in this study, the harmonic balance method is employed to solve (15).

Assume the response solution of (15) is

$$q_1(t) = \sum_{j=1}^{J} A_j + B_j \sin j\omega t, \tag{17}$$

where A_j and B_j are unknown coefficients which are correlative with the static offset and the dynamic amplitude.

Conductor galloping is a low-frequency, high-amplitude wind induced vibration with a single or a few loops of standing waves per span. So assuming the galloping performs a harmonic oscillation, as the initiative approximation the first term of (17) was used in this study. Substituting (17) into (15) and omitting the higher harmonic terms, the following expressions can be derived by making the constant term, the coefficients of $\sin\omega t$ and $\cos\omega t$, respectively, to zero:

$$B_1\left(4C + 3N_4B_1^2\omega^2\right) = 0, \tag{18a}$$

$$2N_2A_1^3 + 2N_1A_1^2 + 2KA_1 + 3N_2A_1B_1^2 + \left(N_1 + N_3\omega^2\right)B_1^2 = 0, \tag{18b}$$

$$B_1\left(12N_2A_1^2 + 8N_1A_1 + 3N_2B_1^2 + 4K - 4\omega^2\right) = 0. \tag{18c}$$

From (18a), the expression of the coefficient B_1 can be obtained as

$$B_1 = 0, \quad \text{or} \quad B_1 = \frac{1}{\omega}\sqrt{-\frac{4C}{3N_4}}, \quad \left(\frac{4C}{3N_4} < 0\right). \tag{19}$$

When $B_1 = 0$, from (18b), the coefficient A_1 can be obtained as

$$A_1 = 0, \quad \text{or} \quad A_1 = \frac{-N_1 \pm \sqrt{N_1^2 - 4KN_2}}{2N_2}, \quad \left(N_1^2 - 4KN_2 \geq 0\right). \tag{20}$$

When $B_1 = (1/\omega)\sqrt{-4C/3N_4}$, from (18c), the coefficient A_1 can be obtained as

$$A_1 = \frac{N_1N_4\omega^4 - \left(N_1N_4K + 6N_2N_3C\right)\omega^2 - 5N_1N_2C}{-3N_2N_4\omega^4 + \left(2N_1^2N_4 - 6N_2N_4K\right)\omega^2 + 15N_2^2C}. \tag{21}$$

Then substituting (19) and (21) into (18b), a higher-order linear equation about the unknown parameter ω can be derived as

$$f(\omega) = Z_1\omega^{12} + Z_2\omega^{10} + Z_3\omega^8 + Z_4\omega^6 + Z_5\omega^4 + Z_6\omega^2 + Z_7 = 0, \tag{22}$$

where $f(\omega)$ is a 12th order polynomial expression (only including even order terms) with respect to ω, $Z_1 - Z_7$ are the coefficients, and there are

$$Z_1 = 9N_2^2N_4^3,$$
$$Z_2 = 3N_2\left(9KN_2N_4^3 - 3N_1^2N_4^3\right),$$
$$Z_3 = -81CN_2^3N_4^2,$$

$$
\begin{aligned}
Z_4 &= 3N_2 \\
&\times \left(-36CKN_1N_2N_3N_4^2 + 3K^2N_1^2N_4^3 \right. \\
&\quad + 6CN_1^2N_2N_4^2 - 12K^3N_2N_4^3 + 8CN_1^3N_3N_4^2 \\
&\quad \left. -18CKN_2^2N_4^2 - 36C^2N_2^2N_3^2N_4 \right), \\
Z_5 &= 3N_2 \left(45C^2N_2^3N_4 + 72CK^2N_2^2N_4^2 \right. \\
&\quad \left. -48CKN_1^2N_2N_4^2 + 8CN_1^4N_4^2 \right), \\
Z_6 &= 3N_2 \left(-135KC^2N_2^3N_4 + 45C^2N_1^2N_2^2N_4 \right), \\
Z_7 &= 225C^3N_2^5.
\end{aligned} \tag{23}
$$

Solving (22) and considering the engineering practice, the effective values of ω are obtained. Returning ω into (19) and (21), the values of A_1 and B_1 can be also obtained.

4. Analysis for Hysteresis Phenomenon

In this section, without loss of generality, a typical conductor type ACSR LGJ-400/35 is selected to analyze the hysteresis phenomenon in the conductor galloping. And physical parameters of the line are tabulated in Table 1. The typical D-shape eccentric ice accretion covered on the conductor is selected in this study. Figure 2 shows the schematic diagrams of the iced conductor cross-section. The ice thickness is chosen to be equal to 15 mm shown in Figure 2.

4.1. Instability Regions for Conductor Galloping. Figures 3 and 4 give the quasi-steady, aerodynamic force coefficients measured in a wind tunnel for the D-shape iced conductor at the different angle of attack θ. A third-order polynomial is used to fit the experimental data in the range of $-85^\circ \le \theta \le 85^\circ$ and a ninth-order polynomial is also used to fit in the range of $-175^\circ \le \theta \le 175^\circ$. The fitting interval by third-order polynomial is less than that by ninth-order obviously. From the figures, there is a certain discrepancy between experimental data and the third-order fitting results, but no significant difference with the ninth-order fit. And the third-order polynomial cannot capture the data versus whole angles of attacks.

The instability regions relatively to the angle of attack that can excite conductor galloping need to be obtained before the hysteresis phenomenon is studied. According to Lyapunov stability theory, the occurrence of the unsteady solutions of (15) should satisfy the condition, $C < 0$, presented in the literature [1]. Figure 5 presents the different instability regions of the angle θ based on third-order and ninth-order fitting curves shown in Figures 3 and 4. For the D-shape iced conductor, the angle interval of galloping occurrence obtained by using third-order fitting curve is only a part of the results by using ninth-order fitting. The three instability regions derived from the ninth-order fitting curve are I = $[-130^\circ, -119^\circ]$, II = $[-18^\circ, 18^\circ]$, and III = $[119^\circ, 130^\circ]$, in which region I is symmetrical distribution with 0°. And the only one region obtained by third-order fitting curve is I = $[-18^\circ, 18^\circ]$.

Table 1: Physical parameter of the conductor type LGJ-400/35 employed in this analysis.

Parameters	Notation	Units	Data
Elastic modulus	E	GPa	76.5
Diameter of conductor	D	mm	26.82
Horizontal initial tension	T_0	kN	25.92
Span length	l	m	500
Cross-section area	A	mm^2	425
Mass of unit length	m	kg/m	1.349
Damping ratio	ξ		0.004

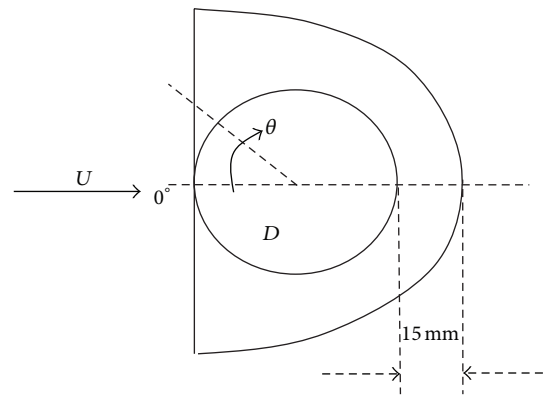

Figure 2: Schematic diagrams of the D-shape iced conductor.

4.2. Influence of the Different Factors on the Hysteresis Phenomenon. It is very known that the hysteresis phenomenon is characterized by the existence of a solution that can alternately reach different cycles limits in theory. In this study, the hysteresis region in the conductor galloping is analyzed by the solutions of the dynamic amplitude B_1 versus the horizontal wind velocity U obtained by (18a), (18b), and (18c). The hysteresis characteristics are also investigated with respect to different factors such as dynamic angle of attack, span length, initial tension, and conductor mass. And two interesting aspects about the point of the hysteresis phenomenon onset and the size of the hysteresis region are proposed under the different conditions.

(1) Influence of the Dynamic Angle of Attack. Luo et al. [17] and Alonso et al. [28] studied the cause of the hysteresis phenomenon in transverse galloping of the square and the triangular cross-section bodies, respectively. Their studies revealed that the cause of the hysteresis phenomenon is related to the point of inflection that exists in the aerodynamic force coefficient curve versus the angle of attack. And Barrero-Gil et al. [27] later proved that the hysteresis phenomenon is related to the number of inflection points.

From Figure 4, three inflection points can be observed using the ninth-order fitting curve, which are evenly distributed in the three instability ranges. And one inflection point is found from the third-order fitting curve in its

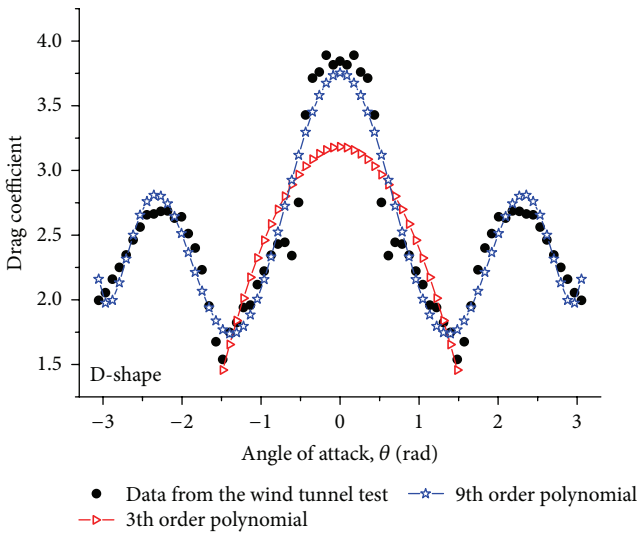

Figure 3: Drag coefficients of the D-shape iced conductor.

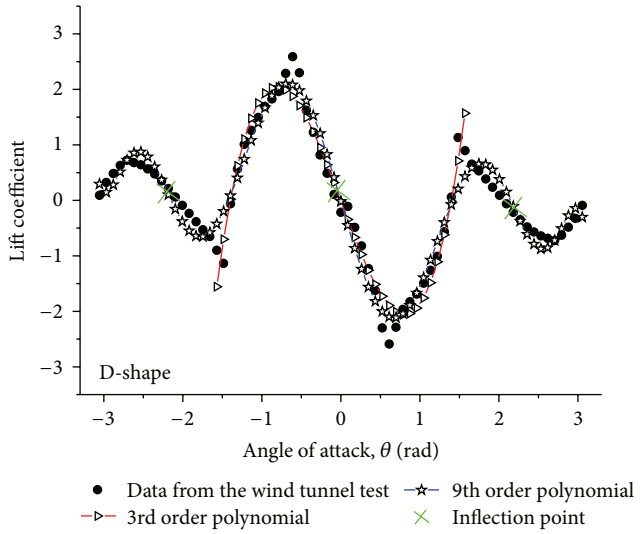

Figure 4: Lift coefficients of the D-shape iced conductor.

only one instability range. Then hysteresis characteristics in the conductor galloping are obtained in each instability range based on the physical parameters presented in Table 1. Figure 6 shows the amplitude B_1 versus the horizontal wind velocity U with several typical angles of attack in the instability interval I. From Figure 6, we can see that the hysteresis characteristic presents a symmetric distribution based on the middle of the instability range. At the two ends of the angle interval, $\theta = -130^\circ$ and $\theta = 119^\circ$, the velocities of the hysteresis phenomenon occurrence are much higher than in the middle of the interval and the sizes of the hysteresis regions are also broader than in the middle. In addition, the critical velocity to excite hysteresis phenomenon is very high in comparison with the point of galloping instability. From the results of this example, the critical wind velocities to excite hysteresis phenomenon are all greater than 40 m/s. So under the actual engineering conditions, it is difficult to achieve for the hysteresis phenomenon.

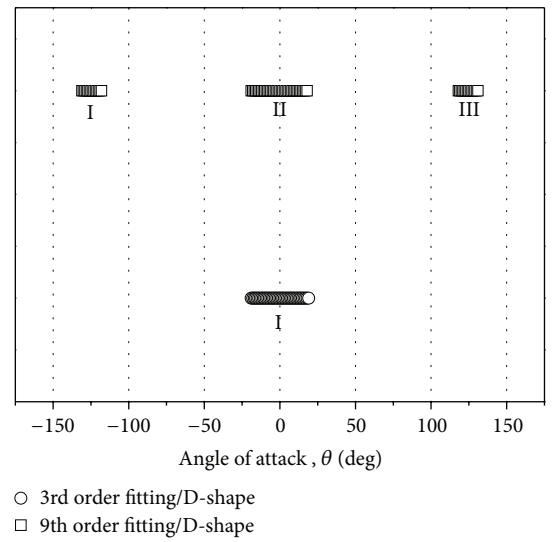

Figure 5: Instability regions for the D-shape iced conductor based on the third-order and ninth-order fitting curves of the aerodynamic force coefficients.

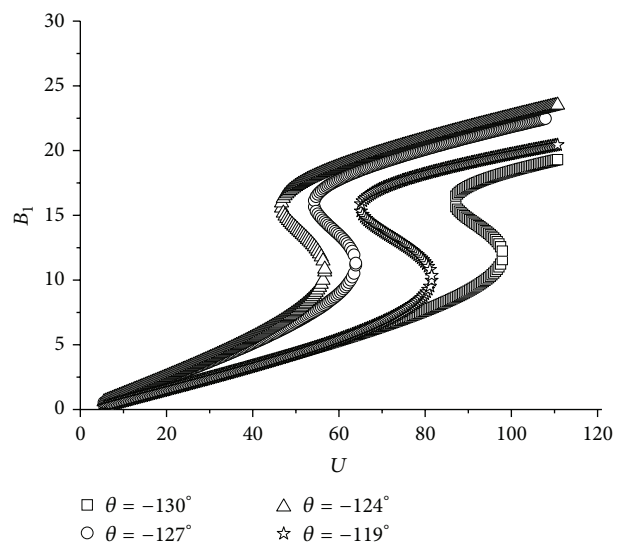

Figure 6: Amplitude B_1 versus horizontal wind velocity U in the instability range I using the ninth-order polynomial.

Figure 7 shows the amplitude B_1 versus the horizontal wind velocity U with several typical angles of attack in the instability interval II. From Figure 7, at the two ends of the angle interval, $\theta = -18^\circ$ and $\theta = 18^\circ$, the velocities of the hysteresis phenomenon occurrence are much higher than in the middle of the interval. The velocities to excite hysteresis phenomenon are lower than in the angle interval I except the ends of the interval. Therefore it is easy to excite the hysteresis phenomenon in this angle interval.

Figure 8 shows the amplitude B_1 versus the horizontal wind velocity U with several typical angles of attack in the instability interval III. Table 2 gives the size of the hysteresis region with respect to different angles of attack. From Table 2, the hysteresis phenomenon obtained in this interval is similar to the characteristics in the interval I presented in Figure 5.

Table 2: The size of the hysteresis region with different angles of attack.

Ninth-order fitting curve						Third-order fitting curve	
Angle interval I		Angle interval II		Angle interval III		Angle interval I	
Angle (°)	Hysteresis range (U, m/s^2)	Angle (°)	Hysteresis range (U, m/s^2)	Angle (°)	Hysteresis range (U, m/s^2)	Angle (°)	Hysteresis range (U, m/s^2)
−130	(87.1, 97.9)	−18	(43.5, 47.9)	119	(73.9, 86.7)	−18	(39.5, 45.5)
−127	(54.3, 63.9)	−12	(21.1, 23.9)	123	(45.9, 55.9)	−12	(21.5, 25.1)
−124	(46.7, 56.7)	0	(15.1, 17.9)	125	(43.1, 53.5)	0	(15.9, 19.1)
−119	(65.1, 81.5)	12	(15.9, 19.5)	130	(59.5, 75.9)	12	(18.7, 22.7)
		18	(31.1, 39.5)			18	(33.1, 40.7)

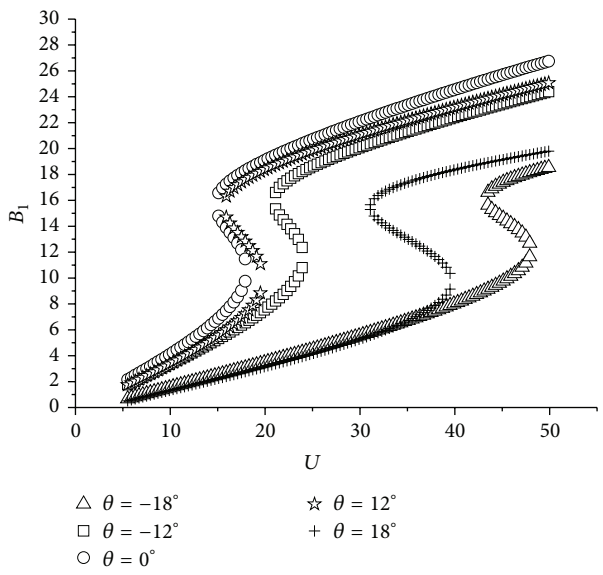

Figure 7: Amplitude B_1 versus horizontal wind velocity in the instability range II using the ninth-order polynomial.

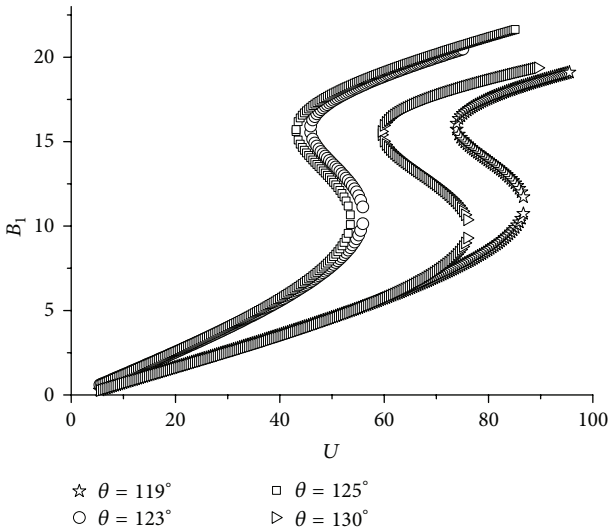

Figure 8: Amplitude B_1 versus horizontal wind velocity in the instability range III using the ninth-order polynomial.

Figure 9 shows the hysteresis phenomenon by using third-order aerodynamic force fitting curve with several typical angles of attack in the interval I presented in Figure 5. This angle interval I is the same of the angle interval II obtained by ninth-order fitting curve shown in Figure 5. From Table 2, the hysteresis region obtained by using the third-order fitting curve is consistent with the result in the same angle of attack from the ninth-order fitting curve.

(2) Influence of the Span Length. In actual engineering structures of overhead transmission lines, the span length has a wide selection range from 100 m to 1200 m, and the common range is from 300 m to 700 m. Select the physical parameters presented in Table 1. Without loss of generality, select ninth-order fitting curve and $\theta = 0^\circ$ presented in Figures 3 and 4 as a typical example.

The effects of span lengths to the hysteresis phenomenon in the conductor galloping are shown in Figure 10. From Figure 10 we can see that when $L < 440$ m, there is no hysteresis phenomenon occurrence on the process of the conductor galloping. And after the hysteresis phenomenon appears when $L = 440$ m, the horizontal wind velocity of the hysteresis onset point increases with the much larger span length, and the hysteresis range makes much wider with the increase of the span length. And in the same wind velocity, before the occurrence of hysteresis phenomenon, the conductor galloping amplitude decreases as the span length increases and the difference is not obvious. But the amplitude jumps abruptly over the hysteresis range and increases obviously as the span length increases.

In addition, when the span length reaches 590 m, a more complex nonlinear vibration phenomenon is excited in the conductor galloping. In the low wind velocity, a secondary bifurcation is presented with an arch-shaped curve. It is likely to be a trend to the chaos. And with the increase of span length this phenomenon is more obvious.

(3) Influence of the Initial Tension. Figure 11 shows the amplitude B_1 versus the horizontal wind velocity U with different initial tensions. The span length is 500 m and the angle of attack is 0°. Other parameters are shown in Table 1. From Figure 11 we can see that the hysteresis phenomenon will be excited with the decrease of the initial tension. And

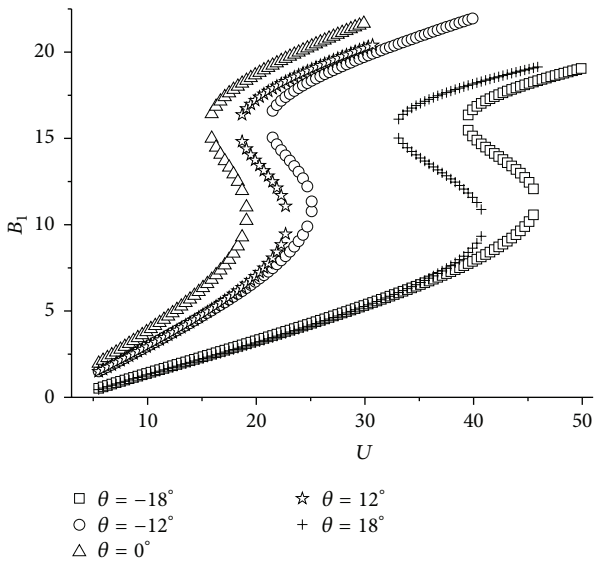

Figure 9: Amplitude B_1 versus horizontal wind velocity in the instability range I using the third-order polynomial.

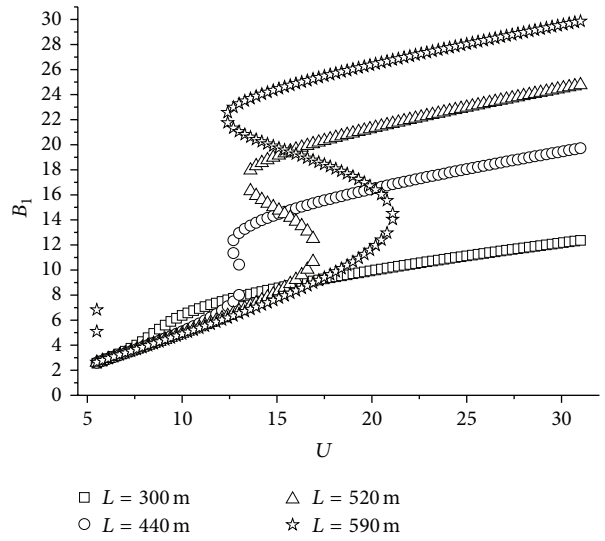

Figure 10: Amplitude B_1 versus horizontal wind velocity with different span lengths.

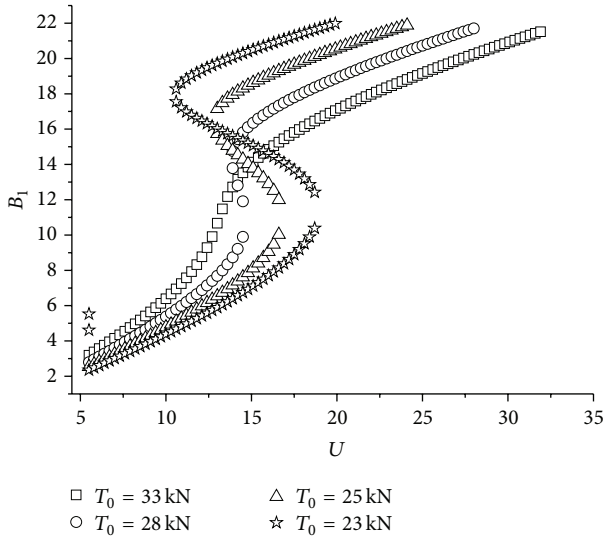

Figure 11: Amplitude B_1 versus horizontal wind velocity with different initial tensions.

when $T_0 = 28$ kN, the hysteresis phenomenon starts to occur in the conductor galloping. The hysteresis range which is characterized by the horizontal wind velocity increases obviously as the initial tension decreases. And in the same wind velocity, before the hysteresis phenomenon occurrence, the conductor galloping amplitude increases as the initial tension increases. But the amplitude jumps abruptly over the hysteresis range and increases obviously as the initial tension decreases. Therefore, it is an approach to control the conductor galloping by selecting a proper initial tension of the transmission line.

In this example, as the initial tension reaches 23 kN, a more complex vibration bifurcation phenomenon is excited in the conductor galloping from Figure 11. It also presents a secondary bifurcation phenomenon. And with the decrease of initial tension, this phenomenon is more obvious.

(4) Influence of the Conductor Mass. Figure 12 shows the amplitude B_1 versus the horizontal wind velocity U with different conductor masses. The span length is 500 m. The angle of attack is 0° and the initial tension is 25.9 kN. Other parameters are shown in Table 1. It should be pointed out that the different masses represent the different conductor types.

From Figure 12 we can see that the hysteresis phenomenon will be excited with the increase of the conductor mass. And when $m = 1.2$ kg/m, the hysteresis phenomenon starts to occur in the conductor galloping. The hysteresis range which is characterized by the horizontal wind velocity increases obviously as the conductor mass increases. And in the same wind velocity, before the occurrence of hysteresis phenomenon, the conductor galloping amplitude decreases as the conductor mass increases. The amplitude jumps abruptly over the hysteresis range and increases obviously as the conductor mass increases. As the conductor mass equals 1.6 kg/m, a more complex vibration bifurcation phenomenon is excited in the conductor galloping from Figure 12. It also presents a secondary bifurcation phenomenon. And with the increase of mass, this phenomenon is more obvious.

5. Conclusions

In this paper, the hysteresis phenomenon in the iced conductor galloping is studied. The analysis is based on a continuum model of the D-shape iced conductor derived by Hamilton principle, in which the initial deformation, the geometric nonlinearity caused by the large deformation, and the aerodynamic nonlinearity are considered. The aerodynamic forces are described by using the quasi-steady hypothesis, where the aerodynamic coefficients are expanded by the polynomial curves with a third order and a ninth order, respectively.

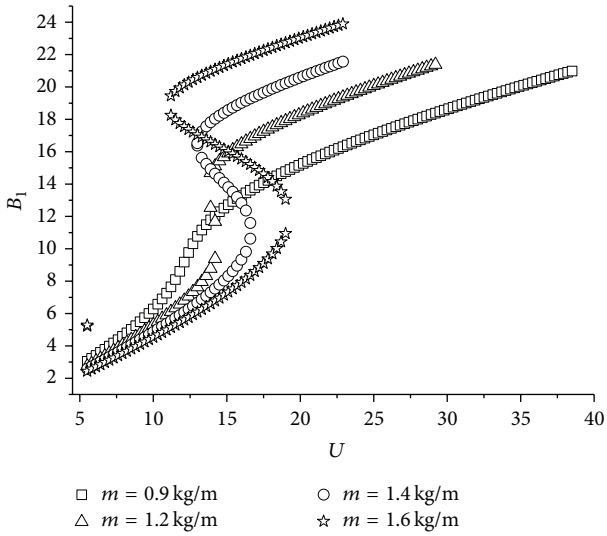

FIGURE 12: Amplitude B_1 versus horizontal wind velocity with different conductor masses.

The hysteresis characteristics are obtained by solving the approximate solutions of the Galerkin discretized equation derived from the continuum model by means of the harmonic balance method. And the influences of the different factors are proposed in different galloping instability intervals.

For the aerodynamic force coefficient curves of the D-shape iced conductor, the fitting interval by the third-order polynomial is less than by the ninth order obviously. The angle interval of galloping occurrence obtained by the third-order fitting curve is only a part of the results by the ninth-order fitting. There are three galloping instability regions derived from the ninth-order fitting curve and there is only one instability region from the third-order fitting curve. Three inflection points are obtained from the ninth-order fitting curve, which are evenly distributed in the three instability ranges. And one inflection point is found from the third-order fitting curve in its only one instability range.

Hysteresis characteristics in the conductor galloping are obtained in each instability range. For the three instability intervals from the ninth-order fitting curve, the velocities of the hysteresis phenomenon occurrence at the two ends of the instability angle interval are much higher than in the middle. Velocities to excite hysteresis phenomenon in the angle interval II are much lower than in the angle intervals I and III expect the ends of the intervals. So under the actual engineering conditions, it is difficult to achieve for the hysteresis phenomenon in the intervals I and III, but easy in the interval II.

The horizontal wind velocity of the hysteresis onset point increases with the much larger span length, and the hysteresis range makes much wider with the increase of the span length. The hysteresis phenomenon will be excited with the decrease of the initial tension, and the hysteresis range which is characterized by the horizontal wind velocity increases obviously as the initial tension decreases. And the hysteresis phenomenon will be excited with the increase of the conductor mass and the hysteresis range increases obviously as the conductor mass increases.

Finally it should be pointed out that only the vertical vibration is considered in order to discuss the hysteresis phenomenon in this study. The torsional motion and the horizontal motion can also have important effects in relation to aerodynamic mechanisms that causes galloping, which will be presented and discussed in our subsequent studies.

Acknowledgment

The authors are grateful for financial support from the National Natural Science Foundation of China (51008288).

References

[1] CIGRE SCB2, WG 11, and Task Force 02.11.06, "State of the art of conductor galloping," Electra 322, Convenor: J. L. Lilien, 2007.

[2] R. D. Blevins, *Flow-Induced Vibration*, Van Nostrand Reinhold, New York, NY, USA, 1990.

[3] Y. L. Guo, G. X. Li, and C. Y. You, *Galloping of the Transmission Line*, China Electronic Power Press, Beijing, China, 2003, (Chinese).

[4] C. B. Rawlins, "Transmission line reference book-wind-induced conductor motion," in *Galloping Conductors*, vol. 792, chapter 4, EPRI Research Project, 1979.

[5] J. P. Den Hartog, "Transmission line vibration due to sleet," *Transactions of AIEE*, vol. 51, part 4, pp. 1074–1086, 1932.

[6] O. Nigol and P. G. Buchan, "Conductor galloping part I: den Hartog mechanism," *IEEE Transactions on Power Apparatus and Systems*, vol. 100, no. 2, pp. 699–707, 1981.

[7] O. Nigol and P. G. Buchan, "Conductor galloping part II: torsional mechanism," *IEEE Transactions on Power Apparatus and Systems*, vol. 100, no. 2, pp. 708–720, 1981.

[8] P. Yu, A. H. Shah, and N. Popplewell, "Inertially coupled galloping of iced conductors," *Journal of Applied Mechanics, Transactions ASME*, vol. 59, no. 1, pp. 140–145, 1992.

[9] P. Yu, Y. M. Desai, A. H. Shah, and N. Popplewell, "Three-degree-of-freedom model for galloping. Part 1: formulation," *Journal of Engineering Mechanics*, vol. 119, no. 12, pp. 2404–2425, 1993.

[10] P. Yu, N. Popplewell, and A. H. Shah, "Instability trends of inertially coupled galloping. Part II: periodic vibrations," *Journal of Sound and Vibration*, vol. 183, no. 4, pp. 679–691, 1995.

[11] C. Ziller and H. Ruscheweyh, "A new approach for determining the onset velocity of galloping instability taking into account the nonlinearity of the aerodynamic damping characteristic," *Journal of Wind Engineering and Industrial Aerodynamics*, vol. 69-71, pp. 303–314, 1997.

[12] A. Luongo and G. Piccardo, "Non-linear galloping of sagged cables in 1:2 internal resonance," *Journal of Sound and Vibration*, vol. 214, no. 5, pp. 915–936, 1998.

[13] G. A. Vio, G. Dimitriadis, and J. E. Cooper, "Bifurcation analysis and limit cycle oscillation amplitude prediction methods applied to the aeroelastic galloping problem," *Journal of Fluids and Structures*, vol. 23, no. 7, pp. 983–1011, 2007.

[14] Z. H. Qin, Y. S. Chen, X. P. Zhan, B. Liu, and K. J. Zhu, "Research on the galloping and anti-galloping of the transmission line," *International Journal of Bifurcation and Chaos*, vol. 22, no. 2, Article ID 1250038, 2012.

[15] K. G. McConnell and C.-N. Chang, "A study of the axial-torsional coupling effect on a sagged transmission line," *Experimental Mechanics*, vol. 26, no. 4, pp. 324–329, 1986.

[16] K. E. Gavronski, *Non-linear galloping of bundle-conductor transmission lines [Ph.D. thesis]*, Clarkson College of Technology, 1977.

[17] S. C. Luo, Y. T. Chew, and Y. T. Ng, "Hysteresis phenomenon in the galloping oscillation of a square cylinder," *Journal of Fluids and Structures*, vol. 18, no. 1, pp. 103–118, 2003.

[18] P. Hémon and F. Santi, "On the aeroelastic behaviour of rectangular cylinders in cross-flow," *Journal of Fluids and Structures*, vol. 16, no. 7, pp. 855–889, 2002.

[19] T. Tamura and Y. Itoh, "Unstable aerodynamic phenomena of a rectangular cylinder with critical section," *Journal of Wind Engineering and Industrial Aerodynamics*, vol. 83, pp. 121–133, 1999.

[20] G. Alonso, J. Meseguer, and I. Pérez-Grande, "Galloping instabilities of two-dimensional triangular cross-section bodies," *Experiments in Fluids*, vol. 38, no. 6, pp. 789–795, 2005.

[21] G. Alonso and J. Meseguer, "A parametric study of the galloping stability of two-dimensional triangular cross-section bodies," *Journal of Wind Engineering and Industrial Aerodynamics*, vol. 94, no. 4, pp. 241–253, 2006.

[22] V. D. Pierre and L. Andre, "Galloping of a single conductor covered with a D-section on high-voltage overhead test line," *Journal of Wind Engineering and Industrial Aerodynamics*, vol. 96, pp. 1141–1151, 2008.

[23] P. Parkinson and N. P. H. Brooks, "On the aeroelastic instability of bluff cylinders," *Journal of Applied Mechanics*, vol. 28, pp. 252–258, 1961.

[24] G. V. Parkinson and J. D. Smith, "The square prism as an aeroelastic non-linear oscillator," *Quarterly Journal of Mechanics and Applied Mathematics*, vol. 17, no. 2, pp. 225–239, 1964.

[25] Y. T. Ng, S. C. Luo, and Y. T. Chew, "On using high-order polynomial curve fits in the quasi-steady theory for square-cylinder galloping," *Journal of Fluids and Structures*, vol. 20, no. 1, pp. 141–146, 2005.

[26] J. A. Dunnmon, S. C. Stanton, B. P. Mann, and E. H. Dowell, "Power extraction from aeroelastic limit cycle oscillations," *Journal of Fluids and Structures*, vol. 27, no. 8, pp. 1182–1198, 2011.

[27] A. Barrero-Gil, A. Sanz-Andrés, and G. Alonso, "Hysteresis in transverse galloping: the role of the inflection points," *Journal of Fluids and Structures*, vol. 25, no. 6, pp. 1007–1020, 2009.

[28] G. Alonso, A. Sanz-Lobera, and J. Meseguer, "Hysteresis phenomena in transverse galloping of triangular cross-section bodies," *Journal of Fluids and Structures*, vol. 33, pp. 243–251, 2012.

[29] R. W. Clough and J. Penzien, *Dynamics of Structures*, McGraw-Hill, New York, NY, USA, 1975.

[30] K. S. Wang and G. J. Tang, "Response analysis of nonlinear vibration of overhead power line under suspension chain state," *Journal of Vibration and Shock*, vol. 22, no. 2, pp. 69–72, 2003.

[31] H. M. Irvine and T. K. Caughey, "The line theory of free vibrations of a suspended cables," *Proceeding of the Royal Society of London A*, vol. 341, pp. 299–315, 1974.

[32] A. Luongo, D. Zulli, and G. Piccardo, "A linear curved-beam model for the analysis of galloping in suspended cables," *Journal of Mechanics of Materials and Structures*, vol. 2, no. 4, pp. 675–694, 2007.

[33] L. Wang and G. Rega, "Modelling and transient planar dynamics of suspended cables with moving mass," *International Journal of Solids and Structures*, vol. 47, no. 20, pp. 2733–2744, 2010.